Chapter 2

Pulsar astrophysics

In this chapter the concepts and models used in this study will be discussed. An overview of some of the basic properties of pulsars will be given, followed by a discussion of the various models explaining how the γ-ray radiation in such systems is produced.

2.1 History of pulsars

The first proposal of an astrophysical object composed mainly of neutrons was made by Baade & Zwicky (1934), and they called this object a neutron star (NS). They also proposed that these stars are supported against gravitational collapse by degenerate neutron pressure, in the same way white dwarf stars are supported by degenerate electron pressure, as both electrons and neutrons obey Pauli's exclusion principle. Furthermore, they postulated that these objects would be the remnants of stars destroyed in Type II supernovae. A supernova explosion occurs at the end of a sufficiently massive star's lifespan, when all the star's nuclear fuel has been spent (Padmanabhan, 2001, see Section 2.3 for a detailed discussion of the formation and properties of NSs).

The first detailed models of the structure of NSs were proposed by Oppenheimer & Volkoff (1939), based on earlier work by Tolman (1939). They based their models on the equation of state of a cold Fermi gas in the context of general relativity. One of the major results from this work was that only NSs less massive than $\sim 3M_{\odot}$ could successfully support themselves against gravitational collapse, the so-called Tolman-Oppenheimer-Volkoff limit. Their work, however, was only taken seriously after the discovery of pulsars in 1968, but would later become one of the foundational pieces of the general relativistic theory of stellar structure (Misner et al., 1973).

The small size of NSs, with diameters of around 30 km (Padmanabhan, 2001), coupled with the then contemporary picture in which NSs don't radiate much other than thermal radiation, meant that the chances of identifying a source as an NS were slim. Astronomers knew roughly where to look though, i.e., at the centres of supernova remnants. The first source to be identified as being a supernova from historical records was the Crab nebula. Duyvendak (1942) and Mayall & Oort (1942) concluded that the Crab nebula had to be the remnant of a supernova explosion witnessed by Chinese astronomers in 1054 AD based on its current rate of expansion, location in the sky, and luminosity. It is worth noting here that, while the research was based on the Chinese accounts, other accounts of the same event were later found in Indian, Japanese, and Arab historical records. This association of the Crab nebula with a supernova explosion was acknowledged by Baade (1942),

who added that the nova of 1054 AD was a supernova of type II. Minkowski (1942) agreed with this, and suggested that the central star of the Crab nebula could be the remnant of the exploded star.

Less than two years after the discovery of the first extra-solar X-ray source (Sco X-1) by Giacconi et al. (1962) (thought to be synchrotron radiation from cosmic electrons), Bowyer et al. (1964) reported the detection of a second source, which was detected in the direction of the Crab nebula. The claim that an NS had been found couldn't be made, however, as the source couldn't be identified as being a point source. NSs were expected to appear as point sources, owing to their very small size compared to other stellar mass objects.

The first serious speculation that a rotating NS may be the engine driving the luminous emission from the Crab nebula came from Wheeler (1966). He proposed that the source of energy for the Crab nebula could be a rotating NS with a magnetic field strongly coupled to the surrounding cloud. Pacini (1967,1968) also discussed the conversion of rotational energy into magnetic-dipole radiation, and ultimately into particle motions, in a system such as the Crab nebula.

The idea that the rotation of such an object may have important observational effects was soon ratified by the accidental discovery of the first four radio pulsars by a Cambridge research group, headed by Anthony Hewish, and Gold's subsequent suggestion that these sources were NSs rotating at the pulsation frequency. The actual discovery was made by Jocelyn Bell, a graduate student at the time, and came from data intended to shed light on the angular structure of compact radio sources by observing the scintillation caused by the irregular structure of the interplanetary medium. The first pulsar they observed (later labelled CP 1919, or PSR J1921+2153) manifested as a series of pulses with a period of about 1.337 s, and was promptly followed by the discovery of three more pulsars in a preliminary search conducted by Hewish et al. (1968).

Gold (1968,1969) made his suggestion that pulsars are NSs rotating at the pulsation frequency on the grounds that no other theoretically known astronomical object was capable of such short and consistent periodicities as those observed by Hewish et al. (1968). He further speculated that the radiation originated from the plasma in the corotating magnetosphere. He suggested that the NSs spin down as their rotational energy is radiated away by relativistic particles. The connection between supernovae, NSs, and pulsars was finally cemented by Cocke et al. (1969) after they observed strong optical pulsations from the central star of the Crab nebula. This observation came in addition to the prior detection of non-periodic radio pulses from the star by Staelin & Reifenstein (1968), and was followed by detections of pulsed radiation in X-rays (Fritz et al., 1969) and γ-rays (Hillier et al., 1970) within the span of a year.

The first satellite mission to make a significant contribution to the number of known pulsars was the *Small Astronomy Satellite 1* (or SAS-1, also called *Uhuru*), launched in 1970 and observing the sky in X-rays. The final *Uhuru* catalogue (also called the 4U catalogue) contained 339 new X-ray sources, the majority of which were binary systems containing accretion-powered pulsars, i.e., systems containing NSs which are accreting matter stripped from their binary partner (Forman et al., 1978). The SAS-2 instrument was launched in 1972 and was the first satellite devoted to γ-ray astronomy, observing in the 20 MeV$-$1 GeV range (Fichtel et al., 1975). Detection of γ-ray pulsations from the Crab and Vela pulsars were made using this instrument, as well as observations of some important non-periodic unidentified sources, one of which would turn out to

be Geminga. Kanbach et al. (1980) showed, using COS-B data, that the Vela pulsar's spectrum could be represented by a power law of the form $dN/dE \propto E^{-\alpha}$ with $\alpha = 1.89 \pm 0.06$ for the phase-averaged spectrum. This provided clear evidence for the existence of non-thermal accelerating processes, as thermal processes are characterised by black-body-like spectra.

Confirmation that pulsar magnetic fields were as large as is expected from the simple conservation laws (see Section 2.3) came soon, after Truemper et al. (1978) inferred a magnetic field strength of 5.3×10^{12} G for HER X-1. This inference was the result of the observation of a strong line feature at ~ 58 keV in the object's pulsed X-ray spectrum, which was interpreted as electron-cyclotron emission at the basic frequency of the hot plasma in the rotating NS's magnetosphere.

The majority of pulsar astrophysics research would be focused on the radio and X-ray bands for the next few decades, with a large number of discoveries being made. Some of the more noteworthy missions during that time include ROSAT (or *Röntgensatellit*), with its factor ~ 1000 improvement in sensitivity over *Uhuru* helping provide information on X-ray fluxes for all the pulsars then known; EUVE (or *Extreme Ultraviolet Explorer*), which observed several NSs in soft X-rays; and RXTE (or *Rossi X-ray Timing Explorer*), which studied X-ray binaries.

The next significant γ-ray discoveries would only come after the launch of the EGRET instrument aboard the *Compton Gamma Ray Observatory* (or CGRO) in 1991. The CGRO studied the γ-ray sky between 1991 and 2000. The five new pulsars detected by EGRET (including one weak detection), along with the γ-ray pulsars in the Crab and Vela nebulae, would constitute the entirety of the known γ-ray pulsar population until the launch of the current generation of γ-ray missions, most notably the Large Area Telescope (LAT) aboard the *Fermi* mission.

2.2 The *Fermi* LAT era

The LAT is the primary instrument on board the *Fermi Gamma-ray Space Telescope*, launched on 11 June 2008. *Fermi* LAT is an imaging, wide field-of-view, high-energy γ-ray telescope covering the energy range from 20 MeV to > 300 GeV.

The scientific objectives addressed by *Fermi* LAT include:

- Understanding the high-energy behaviour of γ-ray bursts.
- Using γ-ray observations as a probe of dark matter.
- Using high-energy γ-rays to probe the early universe.
- Understanding the mechanisms of particle acceleration operating in celestial sources, particularly active galactic nuclei, pulsars, and supernovae remnants.

To achieve these objectives, *Fermi* LAT is currently performing an all-sky survey, taking advantage of its large field of view and high sensitivity to scan the entire sky every three hours (Atwood et al., 2009). One of the important results to date of this all-sky survey is the first *Fermi* LAT catalogue of γ-ray pulsars (Abdo et al., 2010c) produced using the first six months of *Fermi* LAT data, and increasing the number of known γ-ray pulsars from at least 6 (Thompson, 2001) to 46. The number of γ-ray pulsars continues to increase and has breached the 120 mark (Abdo et al.,

2013). This dramatic increase offers the first opportunity to study a sizable population of these high-energy objects.

Other significant outputs, relevant to pulsar astrophysics, from *Fermi* LAT include:

- Its discovery of a γ-ray pulsar in the CTA 1 supernova remnant within the first few days of its operation (Abdo et al., 2008).
- The discovery of sixteen previously unknown γ-ray pulsars through blind frequency searches (Abdo et al., 2009b). Previously, γ-ray pulsars had been detected with the use of a radio or X-ray ephemeris. Saz Parkinson et al. (2010) subsequently reported the discovery of eight additional blind-search γ-ray pulsars.
- The first detection at γ-ray energies (above 200 MeV) of a globular cluster, 47 Tucanae (Abdo et al., 2009c), hosting tens of millisecond pulsars (MSPs).
- The firm detection of the first eight γ-ray MSPs, using radio ephemerides (Abdo et al., 2009a).
- High quality data for the Vela, Crab, and Geminga pulsars (Abdo et al., 2009d, 2010a,b,d).
- The discovery of three radio and γ-ray pulsars (all MSPs) among the sources in the *Fermi* LAT unassociated sources list (Ransom et al., 2011).

2.3 Formation and properties of pulsars

A neutron star (NS) is the remnant of a star that has destroyed itself in a Type II supernova explosion. Type II supernovae are the result of stellar core collapse in massive stars that have not yet shed their outer hydrogen layer. They differ from Type Ib and Type Ic supernovae, and are characterised by the presence of hydrogen absorption lines in their spectra. The latter two subtypes are also the result of stellar core collapse, but are associated with stars which have already shed their hydrogen layer before the explosion. Type Ia supernovae occur when white dwarfs in binary systems accrete enough matter to breach the Chandrasekhar limiting mass of about $1.44 M_{\odot}$, making further support against gravitational collapse by electron degeneracy pressure impossible (Padmanabhan, 2001). What is left of the star after a Type II explosion is either an NS or a black hole, depending on the mass of the progenitor star. Stars between approximately $8 M_{\odot}$ and $30 M_{\odot}$ leave an NS behind, while more massive stars leave a black hole behind.

Type II supernova explosions occur as follows. For most of its life, a star is supported against gravitational collapse by radiation pressure. The energy necessary to maintain this pressure is generated by nuclear fusion reactions at the star's core. Initially the fuel for these reactions is hydrogen, but as the star gets older it is forced to burn increasingly heavier elements. In stars lighter than $\sim 8 M_{\odot}$ this process only continues to helium burning, and the star ends its life as a white dwarf, supported by electron degeneracy pressure, and with a core composed mainly of carbon and oxygen. In heavier stars, however, successively heavier elements will be burned until the star's core is mainly composed of iron. The endothermic nature of iron-burning means that no further energy production is possible, and that the star is unable to sustain itself against gravitational collapse. The star's core subsequently collapses, with a large amount of energy being released in

the form of neutrinos as the process of electron capture (or inverse β-decay) becomes important. A $20\,M_\odot$ star will have a photon luminosity of 4.4×10^{38} ergs/s and a neutrino luminosity of 3.1×10^{45} ergs/s during this phase. The stiffening of the collapsing core material, as Pauli's exclusion principle becomes important (and the strong force becomes repulsive), may lead to a 'hydrodynamic bounce'. The resultant outwardly propagating shock blows the outer layers of the star away in a spectacular supernova explosion. In cases where the neutron degeneracy pressure at the core provides insufficient support for the remaining mass, gravitational collapse continues and a black hole is formed. If this is not the case, though, electron capture continues and nuclei disintegrate into nucleons and electrons. The resulting object is an NS and is supported against gravitational collapse by neutron degeneracy pressure (Carroll & Ostlie, 1996).

If it is assumed that the stellar core rotates more or less rigidly during the gravitational collapse, and that its angular momentum is conserved, then the angular speed Ω of the core after the collapse will be

$$\Omega_f \sim \Omega_i \left(\frac{R_i}{R_f}\right)^2, \tag{2.1}$$

where R is the star's radius, and the subscripts i and f denote the initial (before the collapse) and final (after the collapse) values, respectively. For typical values of $R_i \sim 10^{11}$ cm and $R_f \sim 10^6$ cm, this amounts to an increase in angular speed by a factor of $\sim 10^{10}$, yielding rotational periods (P) well within the millisecond to second range.

The magnetic field is similarly amplified during the collapse under the assumption of the conservation of magnetic flux, with the magnitude of $\boldsymbol{B}$ after the collapse being

$$B_f \sim B_i \left(\frac{R_i}{R_f}\right)^2. \tag{2.2}$$

This relation yields a typical magnitude of $\sim 10^{12}$ G for NSs. Stellar core collapse as described above thus leads to a rapidly spinning, highly magnetised NS. These strong magnetic fields play a very important role in the production of radiation in pulsar magnetospheres (see Section 2.5).

The magnitude of the magnetic field at the pole (B_0) in terms of the pulsar's rotational period P and its time derivative $\dot{P}$ can be derived by equating the rate at which the pulsar's rotation is slowing down and the vacuum magnetic dipole radiation loss rate (Ostriker & Gunn, 1969):

$$\dot{E}_{\rm rot} \equiv \frac{\mathrm{d}}{\mathrm{d}t}\left(\frac{1}{2} I \Omega^2\right) = I \Omega \dot{\Omega} = -\frac{2}{3c^3} \mu^2 \Omega^4 \sin^2 \alpha, \tag{2.3}$$

where $\mu \equiv B_0 R^3/2$ is the magnetic moment, $I \sim MR^2$ the moment of inertia, α the angle between the magnetic and spin axes, and c the speed of light in a vacuum. Solving for B_0 and inserting typical values of $I = 10^{45}$ g.cm^2, $R = 10^6$ cm, and $\alpha \sim 90^\circ$ yields

$$B_0 = \frac{\sqrt{6c^3 I}}{2\pi R^3 \sin\alpha} \cdot \sqrt{P\dot{P}} \simeq 6.4 \times 10^{19} \sqrt{P\dot{P}}, \tag{2.4}$$

in Gaussian units.

To put this relation into the proper context, it is useful to consider how constant-B_0 lines manifest themselves on a P-$\dot{P}$ diagram such as that shown in Figure 2.1. The P-$\dot{P}$ diagram is the

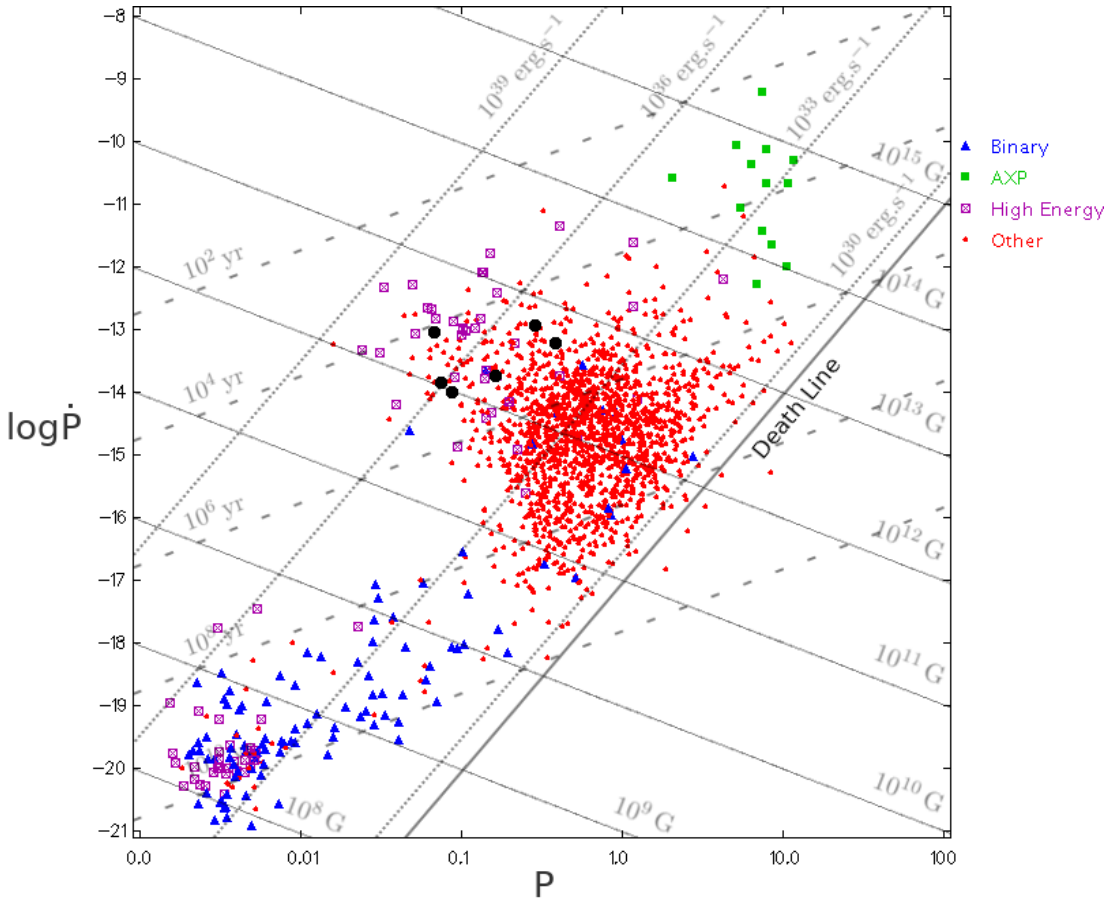

Figure 2.1: A plot of $\dot{P}$ vs. P for all the pulsars in the ATNF pulsar catalogue at the time of writing (http://www.atnf.csiro.au/people/pulsar/psrcat/). The black dots indicate the locations of the six pulsars relevant to this study. Lines of constant B_0 (solid), τ (dashed), and $\dot{E}$ (dotted), as well as the so-called death line, are shown. This death line delimits the border of the so-called 'graveyard', where $\dot{E}$ is too low for pair production to occur (see Section 2.5.2). For a discussion of each of the various types of pulsar indicated on this plot, see Section 2.4.

pulsar equivalent to the HR-diagram in Astrophysics, indicative of pulsar population properties and evolution. By squaring both sides of the relation obtained in Eq. (2.4) and taking the logarithm, it is possible to obtain an expression for the shape of the constant-B_0 lines:

$$\log_{10} \dot{P} = -\log_{10} P + C_1, \tag{2.5}$$

where $C_1 \equiv 2\log_{10}(B_0/(6.4 \times 10^{19}))$ is a constant if B_0 is a constant. Lines of constant B_0 are thus straight lines with negative slope on the P-$\dot{P}$ diagram. In Figure 2.1 it can be seen that the estimation made for the value of B_0 from Eq. (2.2) agrees well with the values derived from observations for the canonical pulsars using Eq. (2.4) (the largest clump in Figure 2.1, see Section 2.4 for more details).

Another quantity that can be derived from Eq. (2.3), is the so-called characteristic age τ. If it is assumed that $\mu_\perp \equiv \mu \sin\alpha$ remains constant throughout the lifetime of the pulsar, then the quantity $P\dot{P}$ also remains constant (as can be seen from Eq. (2.4)). Rewriting the identity $P\dot{P} = P\dot{P}$ as $P\mathrm{d}P = P\dot{P}\mathrm{d}t$, and integrating over the lifetime of the pulsar, the rotational age is found to be

$$\tau = \frac{\left(P^2 - {P_0}^2\right)}{2P\dot{P}} \simeq \frac{P}{2\dot{P}}, \tag{2.6}$$

where it has also been assumed that $P_0 \ll P$, P_0 being the initial period. Predictions made using this relation are in good agreement with the known age of the pulsar in many cases, e.g. the Crab pulsar, where it predicts[1] an age of 1241 yrs as compared to the known age of 958 yrs (Duyvendak, 1942; Mayall & Oort, 1942). In a similar fashion to that by which Eq. (2.5) was constructed, it can be shown that for lines of constant age

$$\log_{10} \dot{P} = \log_{10} P - C_2, \tag{2.7}$$

where $C_2 \equiv \log_{10} 2\tau$. Therefore, lines of constant age are straight and have positive slopes on the P-$\dot{P}$ diagram. Thus, under the assumptions made above, the evolutionary track of a pulsar on the P-$\dot{P}$ diagram roughly proceeds along a line of constant B_0 toward the lower right of the diagram, with the cessation of emission from the pulsar occurring once it crosses the death line. It should be noted, however, that this analysis only applies to rotation-powered pulsars (where Eq. (2.3) holds), and consequently does not account for the properties of accretion-powered pulsars or millisecond pulsars (MSPs).

2.4 Types of pulsars

As the number of known pulsars grew, different populations of pulsars emerged with distinct sets of characteristics. The distinction which is probably most obvious from the P-$\dot{P}$ diagram in Figure 2.1 is that between canonical pulsars and MSPs. These two groups constitute the majority of pulsars in the large cluster in the middle of Figure 2.1, and the smaller cluster in the bottom left corner, respectively. As the name of the latter group suggests, the distinction is made on the basis of rotational period, with pulsars having periods less than approximately 50 ms being classified as MSPs. These faster rotating pulsars are generally older, and have weaker spin-down rates (lower $\dot{P}$). MSPs attain their high rotational velocities through a spin-up process involving a binary partner. The majority of pulsars start their lives as canonical pulsars (in the large cluster) from where their evolution takes them toward the lower right of the P-$\dot{P}$ diagram diagram where they eventually cross the so-called "death line". In the case of MSPs this flow of events is interrupted when the pulsar's binary partner expands enough to trespass on the pulsar's Roche lobe, resulting in the accretion of matter from the binary partner onto the NS's surface. The accretion imparts additional angular momentum onto the pulsar and it is spun up to very short periods. This accretion process not only affects the period of the pulsar, but also the magnetic field, significantly reducing it. MSPs have magnetic fields $\sim 10^8$ G. The most important effect of this weaker magnetic field is that it leads to a considerably lower $\dot{P}$ ($\sim 10^{-20}$ vs. $\sim 10^{-14}$). These short P and low $\dot{P}$ mean that MSPs lose their angular momentum much more slowly than canonical pulsars, and are consequently visible for much longer time-spans. The pulsars in the bridge between the canonical and MSP clusters are pulsars either undergoing spin-up, or pulsars whose binary companions have

[1] As computed at the time of writing using values obtained for P (0.03308471603 s) and $\dot{P}$ (4.22765×10^{-13} s/s) for the Crab pulsar (PSR B0531+21) from the ATNF pulsar catalogue.

ceased accreting matter onto them. The supernova death of the binary companion can result in the pulsar becoming an isolated star, either by the companion completely destroying itself, or by a fatal disruption of the binary system, possibly explaining the existence of isolated MSPs (Shapiro & Teukolsky, 1983).

These two groups aren't, however, the only groups of pulsars which can be characterised by their periods. Anomalous X-ray pulsars (AXPs) and soft γ-ray repeaters (SGRs) are pulsars characterised by their extremely strong magnetic fields and very long periods (up to 10 s), shown in Figure 2.1 as green squares (note that only AXPs are present in Figure 2.1 as it shows only pulsars visible in radio). These sources are thought to be associated with so-called magnetars: objects that experience a very brief period of angular acceleration during their formation due to a strong magnetohydrodynamic dynamo action taking place interior to the star's surface prior to the establishment of a stable configuration. This phenomenon only occurs in stars with very rapid initial rotations $\sim$1 ms. The decay of the immensely strong magnetic fields of these objects powers their radiation, as opposed to the rotation-powered case, and consequently they are only visible for a relatively short period of time (Duncan & Thompson, 1992).

Beyond their periods and magnetic field strengths, pulsars can also be classified by the energy band, or bands, in which they are visible. The simplest example of such a group (and the largest) is that of the radio pulsars. Radio pulsars make up the majority of the known (and of the canonical) pulsars. These pulsars are usually found by performing Fourier-space searches in large sets of radio data, and display a wide variety of pulse profile shapes. A related class are the so-called rotating radio transients (RRATs), which are sources of short, moderately bright radio pulses. These sources may possibly be radio pulsars with larger than usual pulse-to-pulse variability (McLaughlin et al., 2006). Another such group is the γ-ray pulsars, with the vast majority of its members being discovered by using radio periods of known pulsars to fold data obtained from the *Fermi* LAT instrument. These pulsars display a wide variety of pulse profiles, ranging from sharp two-peak profiles to broad single-peak profiles. These pulsars also form part of a larger group, the so-called high-energy pulsars, which also includes those pulsars visible in X-rays. The emission from these pulsars is predominantly curvature radiation (CR) and synchrotron radiation (SR). In Figure 2.1 the purple crossed squares denote the high-energy pulsars.

The last group visible in Figure 2.1 (the blue triangles) is the binary pulsars. In most cases the systems in this class contain an NS and a normal star counterpart, but some instances of NS-NS and NS-black hole binaries have been observed. These binary systems composed of two compact objects have proved useful in tests of general relativity, and are thought to potentially be some of the strongest gravitational wave sources in the universe.

The pulsars in this study are indicated in Figure 2.1 by black dots, and are all high-energy canonical pulsars, visible in both the radio and γ-ray bands. As reported by Weltevrede et al. (2010), they all exhibit roughly single-peak structures in their γ-ray light curves within current statistics. The rotational and derived parameters for these pulsars as reported by Weltevrede et al. (2010) are summarised in Table 2.1.

Table 2.1: Rotational and derived parameters for the six pulsars. Adapted from Weltevrede et al. (2010).

Pulsar (J2000)	Pulsar (B1950)	P (s)	$\dot{P}$ ($10^{-14}\,\mathrm{s.s^{-1}}$)	τ_c ($10^3\,\mathrm{yr}$)	B_0 ($10^{12}\,\mathrm{G}$)	$\dot{E}$ ($10^{35}\,\mathrm{erg.s^{-1}}$)
PSR J0631+1036		0.288	8.29	43.6	5.55	1.73
PSR J0659+1414	B0656+14	0.385	5.50	111	4.66	0.38
PSR J0742−2822	B0740−28	0.167	1.69	157	1.69	1.43
PSR J1420−6048		0.068	8.29	13.0	2.41	104
PSR J1509−5850		0.089	0.92	154	9.14	5.15
PSR J1718−3825		0.075	1.33	89.5	1.01	12.5

2.5 The γ-ray emission models

The main purpose of this study is to investigate the properties of a number of geometric models for the locations of the emitting regions inside pulsar magnetospheres in both the radio and γ-ray cases. To accomplish this effectively it is useful to have an understanding of the fundamental principles that govern the physical models that underlie the geometric models. In this section the 'standard model' of the pulsar magnetosphere is presented, as well as an account of the important emission mechanisms involved in the generation of γ-rays in pulsar magnetospheres. The polar cap (PC), slot gap (SG), and outer gap (OG) models for the production of γ-rays are also presented, with special emphasis on the details which will be most relevant when considering the geometric models.

2.5.1 The Goldreich-Julian pulsar model

Following the suggestion made by Gold (1968) that the newly discovered objects subsequently known as pulsars were rotating magnetic NSs, Goldreich & Julian (1969) investigated the simple case of an aligned rotator, and concluded that a rotating magnetic NS cannot be surrounded by a vacuum.

Consider, as Goldreich & Julian (1969) did, an NS with a dipole external magnetic field continuous at the stellar surface. Assume that the pulsar is a uniformly magnetised, perfectly conducting sphere and its interior field is $\boldsymbol{B}_\mathrm{in} = B_0 \boldsymbol{e}_\mathrm{z} \| \boldsymbol{\mu}$. The alignment of the spin and magnetic axes lead to a static external field. This means that charged particles in the interior of the star will experience a Lorentz force due to the rotation of the pulsar. Under the assumption that the star is a perfect conductor, charge redistribution has to take place to establish counterbalancing electric fields $\boldsymbol{E}$ due to charge separation. No permanent current flow exists inside the star as $\boldsymbol{E}_\mathrm{in} \cdot \boldsymbol{B}_\mathrm{in} = 0$ for a conductor. This implies that the rotational form of Ohm's law applies, thus

$$\boldsymbol{E}_\mathrm{in} = -\frac{1}{c}\left[(\boldsymbol{\Omega} \times \boldsymbol{r}) \times \boldsymbol{B}_\mathrm{in}\right] = -\frac{\Omega B_0 r \sin\theta}{c}\left(\sin\theta \boldsymbol{e}_\mathrm{r} + \cos\theta \boldsymbol{e}_\theta\right), \tag{2.8}$$

where r and θ (and ϕ) are spherical coordinates centred on the NS. This interior electric field obeys the condition $\boldsymbol{\nabla} \times \boldsymbol{E}_\mathrm{in} = 0$, and solving Laplace's equation yields an external electrostatic potential (assuming that $\boldsymbol{E}$ is continuous at the stellar surface)

$$\Phi = -\frac{B_0 \Omega R^5}{3cr^3} \mathrm{P}_2(\cos\theta), \tag{2.9}$$

where P_2 is the Legendre polynomial of second degree. In the case where the pulsar is surrounded by a vacuum, this potential implies an external value for the Lorentz invariant $\boldsymbol{E} \cdot \boldsymbol{B}$, such that

$$\boldsymbol{E} \cdot \boldsymbol{B} = -\left(\frac{\Omega R}{c}\right)\left(\frac{R}{r}\right)^7 {B_0}^2 \cos^3\theta \neq 0. \tag{2.10}$$

This quantity vanishes in the stellar interior. This means that this quantity must change continuously from its interior value to its exterior value within the surface charge layer. As the exterior value is not zero there is a non-zero component of the electric field parallel to the magnetic field ($\boldsymbol{E}_{\parallel}$) at the surface of the NS. For typical pulsar parameters the force associated with this component is many orders of magnitude larger than the gravitational binding force acting on charged particles at the surface ($\sim 10^8$ times larger for a proton). Consequently the particles at the stellar surface cannot be in dynamical equilibrium, and will be pulled from the surface of the NS.

Goldreich & Julian (1969) further showed that the charge density in the co-rotating magnetosphere is

$$\rho_{\rm GJ} = \frac{1}{4\pi}\boldsymbol{\nabla} \cdot \boldsymbol{E} \simeq -\frac{1}{2\pi c}\boldsymbol{\Omega} \cdot \boldsymbol{B}, \tag{2.11}$$

also known as the Goldreich-Julian charge density. This relation implies the existence of a so-called null-charge surface, where the local charge density is zero. This surface is made up of all the points inside the corotating region where $\boldsymbol{\Omega} \cdot \boldsymbol{B} = 0$, and it separates the magnetosphere into positively and a negatively charged regions. In the case of an aligned rotator there are two negatively charged regions, one above each PC, and one positively charged region, around the star's equator (see Figure 2.2). Goldreich & Julian (1969) also stated that no particles can corotate beyond the so-called light cylinder with radius $R_{\rm LC} \equiv c/\Omega$ (as measured from the rotation axis) as the velocity of a corotating particle outside this cylinder would necessarily exceed the speed of light. There will therefore be a net outflow of particles through the surface of this cylinder along magnetic field lines that don't close inside it. The magnetic field line that crosses the null-charge surface at the light cylinder is called the critical field line. The resulting picture of the magnetosphere is shown in Figure 2.2.

In this model, $\boldsymbol{E} \cdot \boldsymbol{B} = 0$ everywhere due to the presence of the conductive plasma (the so-called force-free or ideal magnetohydrodynamic assumption), which means that no particle acceleration due to a non-zero $\boldsymbol{E}_{\parallel}$ will take place, and consequently no radiation will be produced. However, pulsar emission resulting from such acceleration is observed (e.g., Kanbach et al., 1980), which suggests that this model is perhaps too simplified. As will be illustrated in the following sections, models addressing this issue generally have a so-called acceleration gap located somewhere in their magnetosphere where $\boldsymbol{E} \cdot \boldsymbol{B} \neq 0$. The geometric models presented in Chapter 3, which are used in this study, are based on these physical models. These geometric models take only the location of the gaps into account, and not how they come about. It is however important to understand how the relevant emission processes in these physical models operate so as to better motivate the assumptions made in constructing the geometric models.

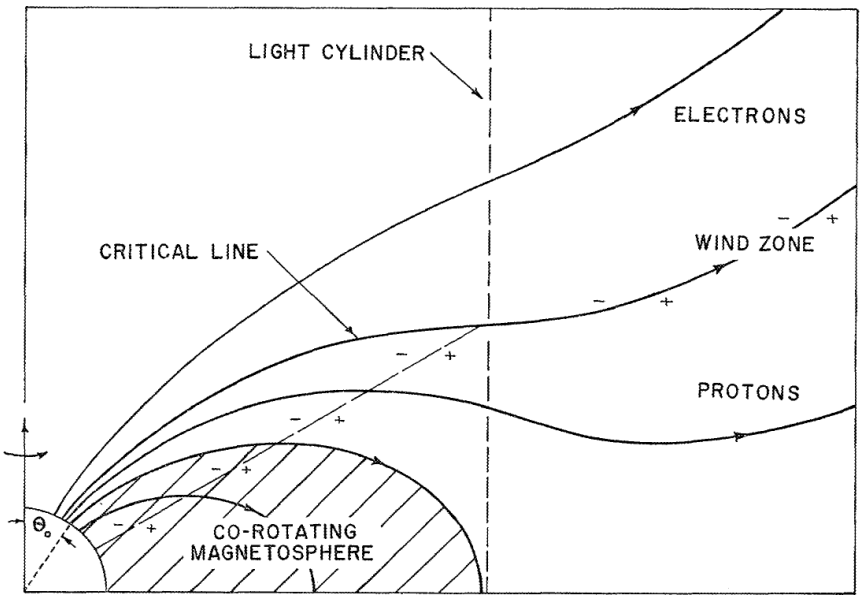

Figure 2.2: Schematic representation of the magnetosphere of an aligned rotator. The NS is at the lower left, and the star's angular velocity vector is directed upward, parallel to its magnetic axis. The PC angle is denoted by θ_0, and corresponds to the location of the footpoints of the last open field lines. The dashed vertical line indicates the light cylinder, while the slanted dashed line indicates the null-charge surface, where $\Omega \cdot \boldsymbol{B} = 0$. The shaded region, within which all magnetic field lines are closed, is called the corotating magnetosphere and is filled with a plasma of charged particles which corotate with the pulsar. Particles stream out through the light cylinder along the open magnetic field lines into the wind zone, with field lines above the critical field line carrying negative charges, and field lines below it carrying positive charges. The charge density inside the light cylinder is described by Eq. (2.11). From Goldreich & Julian (1969).

2.5.2 Emission processes

Synchrotron radiation (SR)

Charged particles moving relativistically through a magnetic field will emit SR. This process is the analogue of cyclotron radiation in the relativistic limit. Neglecting radiation losses, the equations of motion for a particle moving though a uniform magnetic field $\boldsymbol{B}$ are (Rybicki & Lightman, 1979):

$$\frac{d}{dt}\left(\gamma m \boldsymbol{v}\right) = \frac{q}{c}\left(\boldsymbol{v} \times \boldsymbol{B}\right) \tag{2.12}$$

$$\frac{d}{dt}\left(\gamma m c^2\right) = q\left(\boldsymbol{v} \cdot \boldsymbol{B}\right) = 0, \tag{2.13}$$

where $\boldsymbol{v} = \boldsymbol{\beta} c$ is the particle's velocity, q its charge, m its mass, and $\gamma = \sqrt{1 - v^2/c^2}^{-1/2}$ is the Lorentz factor. From the second of these two equations it follows that the particle's γ is constant (and thus too its speed), and from the first it follows that the particle's acceleration is always perpendicular to its velocity. This implies that it will follow a helical path with axis parallel to the magnetic field. The associated gyration frequency is:

$$\omega_B = \frac{qB}{\gamma m c}, \tag{2.14}$$

which is lower by a factor of $1/\gamma$ than it would be in the non-relativistic case (Rybicki & Lightman, 1979).

The radiation emitted by a rapidly moving particle is strongly beamed in its direction of motion. The opening angle of this beam is $\sim \frac{1}{\gamma}$, and the particle's emission thus sweeps out a cone with angle $\alpha = \arctan\left(v_\perp / v_\parallel\right)$. Emission will only be directed towards a fixed observer once per gyration, and the observed pulses will be much smaller than the gyration period by a factor of γ^3. The radiation spectrum emitted by a single electron in this way is uniform up to a cut-off frequency $\omega_c \sim 1/\triangle t$, where $\triangle t \ll t_B$ is the duration of the pulses, and $t_B = 2\pi/\omega_B$ is the gyration period, and is

$$\frac{dP}{d\omega} \equiv P(\omega) = \frac{\sqrt{3}}{2\pi} q^2 \left(\frac{\gamma}{\rho}\right) F\left(\frac{\omega}{\omega_c}\right), \tag{2.15}$$

where $\rho = \gamma m c^2/(qB_\perp)$ is the radius of curvature of the helix, $\omega_c = 3c\gamma^3/2\rho$ is the cut-off frequency, and $F(x)$ is the synchrotron function, which has the following asymptotic forms:

$$F(x) \sim \begin{cases} \frac{4\pi}{\sqrt{3}\Gamma\left(\frac{1}{3}\right)} \left(\frac{x}{2}\right)^{1/3}, & x \ll 1 \\ \left(\frac{\pi}{2}\right)^{1/2} e^{-x} x^{1/2}, & x \gg 1. \end{cases} \tag{2.16}$$

For a single electron this spectrum is well known. It extends as a power law of index 2/3 up to ω_c, beyond which it drops off exponentially in intensity. For the case where the particle energies of a population can be described by a power law with index p, the integrated power spectrum is also a power law $P(\omega) \propto \omega^{-s}$, where $s = (p-1)/2$.

Curvature radiation (CR)

In the limit where the particles are moving along the magnetic field, with no component of velocity perpendicular to it, the radiation produced is somewhat different. The radiation produced by such particles is called CR, and is associated with changes in longitudinal energy with respect to the magnetic field, as opposed to changes in transverse energy in the case of SR. This process is especially important for pulsars, as the particles liberated from the stellar surface (the primary particles, see Section 2.5.1), and subsequently accelerated along the magnetic field lines, have negligible momentum perpendicular to the magnetic field (Sturrock, 1971). These particles emit CR in a cone of opening angle $\sim 1/\gamma$ centred on the magnetic field line, which means that under the extreme acceleration which occurs in NS magnetospheres, this CR is emitted close to tangent to the magnetic field line. This fact is important when constructing the geometric models (see Chapter 3).

The power spectrum for this CR is the same as that for SR for a single particle, but with the modification that ρ is no longer the gyration radius, but the radius of curvature of the magnetic field. For a power law population the resulting spectral index is, however, not the same as for SR due to the curvature radius typically being so much larger than the gyration radius. The spectral index for CR for a power law population is $s = (p-2)/3$, and this spectrum again only extends up to ω_c. It is important to note, however, that this cut-off frequency is much higher for CR than it is for SR due to its dependence on ρ.

Pair production

The photons produced by the radiation processes discussed above may interact with the strong magnetic field of the pulsar to produce electron-positron pairs if they are sufficiently energetic. The probability of a photon with a frequency ν, having energy $h\nu \gtrsim 2m_e c^2$, where m_e is the mass of an electron and c is the speed of light, interacting with the magnetic field to produce an electron-positron pair can be expressed as a photon attenuation coefficient $\alpha(\chi)$. This coefficient determines the actual number of pairs n_p created for a photon path length d in a magnetic field B through the relation Erber (1966)

$$n_p = n_\gamma \left(1 - e^{-\alpha(\chi)d}\right) \simeq n_\gamma \alpha(\chi) d, \tag{2.17}$$

where n_γ is the photon number density, the parameter $\chi \equiv \frac{1}{2}(h\nu/m_e c^2)(B_\perp/B_{cr})$ is the Erber parameter, $B_\perp$ is the component of the magnetic field perpendicular to the particle's direction of motion, and $B_{cr} = m_e^2 c^3/e\hbar = 4.414 \times 10^{13}$ G is the critical magnetic field in which the gyro energy of an electron (or positron) would be equal to its rest mass (Daugherty & Harding, 1983). This coefficient, which corresponds to the photon absorption per unit length when considering photon propagation perpendicular to a uniform, unbounded magnetic field, is given by (Erber, 1966)

$$\alpha(\chi) = \frac{1}{2}\left(\frac{\alpha_f}{\lambda_c}\right)\left(\frac{B_\perp}{B_{cr}}\right) T(\chi), \tag{2.18}$$

where $\alpha_f = e^2/\hbar c \approx 1/137$ is the fine structure constant, λ_c is the Compton wavelength, and $T(\chi)$ is a dimensionless auxiliary function with the following asymptotic forms:

$$T(\chi) = \begin{cases} 0.46 e^{-\frac{4}{3\chi}}, & \chi \ll 1 \\ 0.60\,(\chi)^{-1/3}, & \chi \gg 1. \end{cases} \tag{2.19}$$

Using the approximation for $T(\chi)$ where $\chi \ll 1$, appropriate for pulsars, Eq. (2.18) becomes (Luo et al., 2000)

$$\alpha(\chi) = 0.46 \left(\frac{\alpha_f}{\lambda_c}\right)\left(\frac{\chi}{\epsilon_\gamma}\right) e^{-\frac{4}{3\chi}}, \tag{2.20}$$

where ϵ_γ is the photon energy. Thus, $\alpha(\chi) \sim \chi e^{-\frac{1}{\chi}}$, which means that as $B_\perp$ is increased, and therefore χ, the magnetic field opacity also increases for a constant ϵ_γ. This implies that sufficiently strong magnetic fields are in principle completely efficient pair producers for photons of arbitrarily high energy.

2.5.3 The polar cap (PC) model

In the PC model of Daugherty & Harding (1982), charged particles are liberated from the PC surface by the strong electric field component parallel to the local magnetic field, $\boldsymbol{E}_\parallel$. They are accelerated extremely rapidly along the curved magnetic field lines, producing CR very close to the PC surface. If the emitted photons are energetic enough, they will produce $e^\pm$ pairs via single photon pair production (discussed in Section 2.5.2). These secondary particles will generally have a component of their velocity perpendicular to the magnetic field, and will subsequently produce SR, radiating

the kinetic energy associated with this perpendicular component away over a very short time-scale. The two oppositely charged members of each pair will also be accelerated in opposite directions along the magnetic field lines by $\boldsymbol{E}_{\parallel}$. The stream of inwardly accelerated particles produced in this way (typically positrons for $\alpha < 90°$) heat the PC by means of their collisions with it, which then drives the further thermionic emission of charged particles from the stellar surface (Harding & Muslimov, 2003). The outwardly accelerated particles also produce CR, which then leads to the production of yet more $e^{\pm}$ pairs, and so forth. Thus a single liberated primary particle leads to a cascade of charged particles as depicted in Figure 2.3.

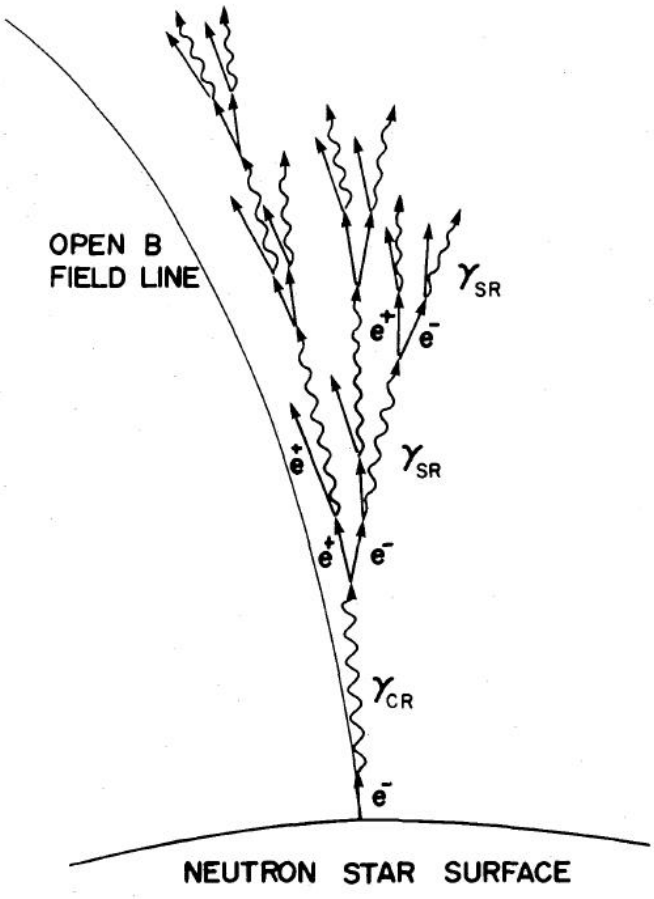

Figure 2.3: Schematic representation by Daugherty & Harding (1982) of a pair photon cascade resulting from the acceleration of a primary electron along the curved magnetic field of an NS. Four generations of photons, including both CR photons ($\gamma_{\rm CR}$) and SR photons ($\gamma_{\rm CR}$) are shown. The kinetic energy of the produced particles associated with motion perpendicular to the magnetic field is almost instantaneously radiated in the form of SR due to the strong magnetic field.

The plasma of charged particles produced in this way increases in number density as one moves farther away from the stellar surface, becoming sufficiently dense to screen $\boldsymbol{E}_{\parallel}$ above the so-called pair formation front (PFF). The resulting magnetosphere is one in which particles are accelerated close to the PC, with a pair-plasma coasting outward relativistically above the PFF. Any colatitudinal dependence of the PFF altitude above the PC is neglected. Thus the PFF is taken to be one-dimensional, i.e., at a constant altitude above the NS surface over the whole PC, with the emission responsible for the observed LCs originating below it.

2.5.4 The slot gap (SG) model

The SG model (Arons, 1983), which serves as the basis for the geometric TPC model, is in a sense an extension of the PC model. In the PC model the height of the PFF above the polar cap is taken to be the same over the whole PC. The SG model considers the two-dimensional structure of the PFF, specifically how its height above the PC depends on colatitude. Arons (1983) found that as one moves closer to the last open field line, the height at which the PFF is encountered increases, until it practically extends all the way to the light cylinder along the last open field line.

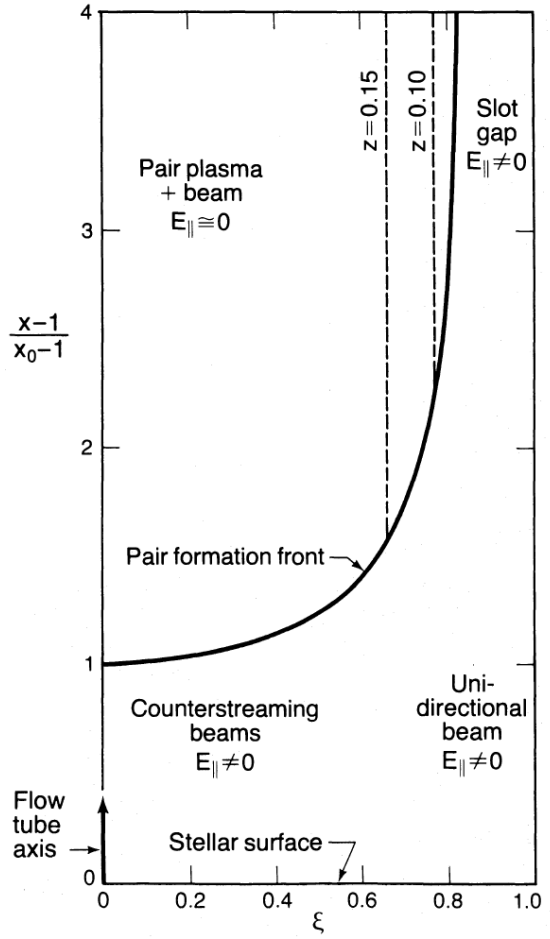

Figure 2.4: Meridional cross-section of an axisymmetric PFF. The solid line indicates the position of the PFF (expressed in units of the height of the PFF directly above the centre of the PC) as a function of distance away from the magnetic axis (expressed as a fraction of the angular distance to the footpoint of the the last open field line). In this figure the left-most axis corresponds to the magnetic axis, and the right-most axis corresponds to the last open field line. In the region above the PFF the electric field has no vertical component (i.e., parallel to the magnetic field), as it is quenched by the charged particle plasma produced in the pair-production cascade. In the region below the PFF this is not the case, and particles can still be accelerated (Arons, 1983).

Consider a pulsar magnetosphere in which the closed field line region is filled with plasma, and particles are streaming out from the NS surface, but no pair production cascade has ensued. In this picture there exists a region with a non-zero $\boldsymbol{E}_{\parallel}$ above the PC, and a region in which $\boldsymbol{E}_{\parallel}$ is zero (the closed field line region). As there should not be any discontinuities in the electric field, it can be inferred that the electric potential along the magnetic field lines inside the open field line region has a maximum somewhere inside this region, and decreases as one moves toward the interface between the two regions, finally becoming zero at the interface itself. This translates into

the picture presented by Arons (1983) when considering the effect this boundary condition has on the magnitude of the acceleration experienced by particles in the open field line region. Weaker acceleration at larger θ, due to the weaker $\boldsymbol{E}_{\parallel}$, implies that a longer acceleration distance is needed for a particle to attain an energy sufficient to produce CR photons, which are in turn energetic enough to produce $e^{\pm}$ pairs, and thus trigger the pair production cascade required to form the PFF. Now including the effect of the pair production cascade, Figure 2.4 shows what this structure looks like, with the PFF closest to the stellar surface directly above the magnetic pole, and increasing in altitude as one moves closer to the last open field line.

2.5.5 The outer gap (OG) model

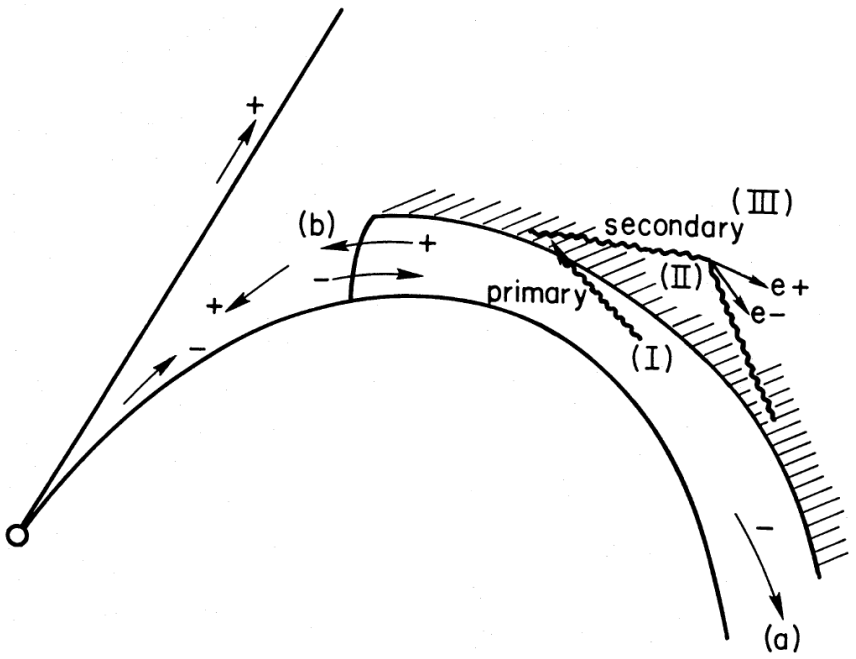

Figure 2.5: Schematic representation of the positions of the primary (**I**), secondary (**II**), and tertiary (**III**) regions associated with the outer gap (see text for details). The current flow along the magnetic field lines begins at (b) and extends through (a). For a pulsar spinning in the opposite direction with the same magnetic field the signs of all the charges will be reversed (Cheng et al., 1986b).

Cheng et al. (1986a,b) postulated a mechanism for the creation and sustenance of significant outer magnetosphere gaps by assuming a global current flow in the pulsar magnetosphere. They considered a situation where the charge density above the PC was positive (Cheng et al., 1986a), which most closely agrees with the case of an anti-aligned rotator in the context of Eq. (2.11). In their model negative charges flow out of the inner magnetosphere along the last open field lines (crossing the light cylinder at *(a)* in Figure 2.5), while positive charges flow out along open field lines closer to the magnetic pole. The outflow of negative charges creates a slab-like region where $\boldsymbol{E} \cdot \boldsymbol{B} \neq 0$ along the last open field line. This region is called an acceleration gap, as particles can be accelerated by the non-zero $\boldsymbol{E}_{\parallel}$ inside it. The processes of SR, CR, pair production, and inverse Compton radiation lead to an eventual steady state configuration consisting of three regions as shown in Figure 2.5. The gap itself extends along the last open field line, from the null-charge surface to beyond the light cylinder (Region **I** in Figure 2.5), and from the last open field line inward

toward the magnetic axis, bounded by the boundary layer (Region **II** in Figure 2.5). The non-zero $\boldsymbol{E}_{\parallel}$ inside the gap means that charges will be accelerated along the magnetic field lines. As these primary particles are accelerated by the large potential in the gap, which can be of the order of $\sim 10^{15}$V (Cheng et al., 1986a) along curved field lines, they emit CR in the form of primary γ-rays. These primary γ-rays subsequently convert, either within the gap or in the boundary layer, into $e^{\pm}$ pairs which are again accelerated by the non-zero $\boldsymbol{E}_{\parallel}$. The charged particles produced inside the gap contribute to the population of primary particles, while the particles produced farther away from the gap, in the boundary layer, are the secondary electrons and positrons. The subsequent separation of these particles, as they are accelerated in opposite directions, eventually sets up a net charge which terminates the gap by quenching the non-zero $\boldsymbol{E}_{\parallel}$.

This quenching does not occur throughout the whole gap, though, but rather occurs in a fashion similar to that in which the non-zero $\boldsymbol{E}_{\parallel}$ near the surface of the NS is quenched in the PC case. The positive curvature of the magnetic field lines, coupled with the assumed tangential emission of the primary γ-rays, means that a produced γ-ray will undergo pair production farther away from the last open field line than where it was produced.

The primary and secondary electrons and positrons produced through pair production have velocity components perpendicular to the local magnetic field, and will produce SR in the form of X-rays (Cheng et al., 1986b), as well as CR in the form of X-rays and γ-rays. The weaker $\boldsymbol{E} \cdot \boldsymbol{B} \neq 0$ of the boundary layer means, however, that the separation of charges is less efficient, with only the fraction needed to establish the gap's "upper" charge boundary being separated. Since the primary electrons and positrons move in opposite directions, so will the primary γ-rays and the secondary pairs they create. This means that the secondary γ-rays and X-rays are emitted in crossed beams, leading to the production of tertiary $e^{\pm}$ pairs in the tertiary pair-filled magnetosphere well beyond the gap (Region **III** in Figure 2.5). Most of these pairs are created with energies far less than what is necessary to produce γ-rays, or even X-rays. The radiation from this region is mainly infrared SR, which floods the entire magnetosphere and plays a very important part in the production of pairs in both regions **I** and **II** through collisions with the primary γ-rays. In addition, these infrared photons could also contribute to the primary γ-ray flux in young pulsars like Vela through inverse Compton collisions with primary particles inside the gap (Cheng et al., 1986b). The secondary γ-rays which do not convert to tertiary $e^{\pm}$ pairs may escape the magnetosphere completely, making up the bulk of the γ-ray emission that would be observed from the pulsar (Cheng et al., 1986b).